geosciences

MDPI

Article

Volcanic Tremor of Mt. Etna (Italy) Recorded by NEMO-SN1 Seafloor Observatory: A New Perspective on Volcanic Eruptions Monitoring

Tiziana Sgroi [1,*], Giuseppe Di Grazia [2] and Paolo Favali [1,3]

[1] Istituto Nazionale di Geofisica e Vulcanologia, 00143 Rome, Italy; paolo.favali@ingv.it
[2] Istituto Nazionale di Geofisica e Vulcanologia, Osservatorio Etneo, 95125 Catania, Italy; giuseppe.digrazia@ingv.it
[3] EMSO ERIC (European Multidisciplinary Seafloor and water-column Observatory European Research Infrastructure Consortium), 00143 Rome, Italy; paolo.favali@emso-eu.org
* Correspondence: tiziana.sgroi@ingv.it; Tel.: +39-06-5186-0582

Received: 22 January 2019; Accepted: 27 February 2019; Published: 5 March 2019

Abstract: The NEMO-SN1 seafloor observatory, located 2100 m below sea level and about 40 km from Mt. Etna volcano, normally records a background seismic signal called oceanographic noise. This signal is characterized by high amplitude increases, lasting up to a few days, and by two typical 0.1 and 0.3 Hz frequencies in its spectrum. Particle motion analysis shows a strong E-W directivity, coinciding with the direction of sea waves; gravity waves induced by local winds are considered the main source of oceanographic noise. During the deployment of NEMO-SN1, the vigorous 2002–2003 Mt. Etna eruption occurred. High-amplitude background signals were recorded during the explosive episodes accompanying the eruption. The spectral content of this signal ranges from 0.1 to 4 Hz, with the most powerful signal in the 0.5–2 Hz band, typical of an Etna volcanic tremor. The tremor recorded by NEMO-SN1 shows a strong NW-SE directivity towards the volcano. Since the receiver is underwater, we inferred the presence of a circulation of magmatic fluids extended under the seafloor. This process is able to generate a signal strong enough to be recorded by the NEMO-SN1 seafloor observatory that hides frequencies linked to the oceanographic noise, permitting the offshore monitoring of the volcanic activity of Mt. Etna.

Keywords: Mt. Etna volcano; oceanographic noise; volcanic tremor; volcanic monitoring by seafloor observatories

1. Introduction

Seafloor and water-column observatories have proved to be excellent tools in long-term monitoring to study processes occurring in hard-to-access abyssal areas [1,2]. Real-time data recorded by seafloor seismic stations have been used to both improve the location of earthquakes occurring in offshore areas and to evaluate the accuracy of eruption mechanisms of both seamounts and sub-aerial volcanoes [3,4]. Since the late 2000s, many programs have begun in Canada, the USA, Japan, Europe, and many other countries to establish permanent underwater infrastructures. In Canada, Ocean Networks Canada (ONC) manages, among other infrastructures, the deep-sea cabled network North East Pacific Time-series Underwater Networked Experiments (NEPTUNE) in the Northeast Pacific Ocean and the shallow-water cabled Victoria Experimental Network Under the Sea (VENUS) in the Salish Sea between Vancouver Island and the continent [5]. In the USA, a network of multiple element hydrophone arrays (NOAA) was deployed for monitoring the seismicity occurring at the Juan de Fuca and Gorda Ridges [6,7]. The installation of the Ocean Observatories Initiative Cabled Array supports near-continuous geophysical monitoring [8]. OOI allows the monitoring of both the volcanic

eruption of the Axial Seamount, focusing on the magma recharge beneath the southeastern part of the summit caldera [9,10], and the offshore earthquakes that are important for understanding Cascadia interplate dynamics [11].

In Europe, the European Multidisciplinary Seafloor and water column Observatory European Research Infrastructure Consortium (EMSO-ERIC) aims to explore the seas around Europe to gain a better understanding of geophysical, geochemical, and environmental phenomena [12]. The NEMO-SN1 multidisciplinary observatory, a node of EMSO ERIC, was deployed in the Western Ionian Sea first in stand-alone configuration and then in cabled mode [13–15]. The NEMO-SN1 was deployed to monitor the offshore seismicity linked to the seismogenic structures that cause the most destructive earthquakes occurring in Italy [16], and to focus on the deep volcanic structures of Mt. Etna [16,17].

Sea dynamics are the source of a typical background seismic signal: oceanographic noise. The origin of this signal may be associated with different causes: the nonlinear interaction of the sea waves with the seafloor bathymetry [18], local atmospheric conditions [19], wave height amplitudes caused by local atmospheric perturbations [20,21], and resonance effects of sedimentary layers [22]. Waves and currents generate seabed disturbances [23] and tides act as trigger of microearthquakes from normal faults [24]. Seismic data recorded by seafloor seismometers are affected by daily and seasonal variations, including ocean loading, bottom currents, and marine organisms, as well as instrumental problems [23–30].

A typical low-frequency seismic signal recorded at active volcano sites around the world is the volcanic tremor, which is associated with the movement of magma, fluids, or gas [31]. Rising gas pockets within the magma column interact with the conduit walls, causing a vibration that produces a tremor signal. This vibration precedes and accompanies the explosive eruption; volcanic tremor plays a significant role in real-time volcano monitoring as the pattern of this signal strongly reflects the evolution of the eruptive activity [32–34]. In recent years, ocean bottom seismometers (OBSs) and seafloor observatories have been used to monitor from the seafloor the volcanic activity of Stromboli [35] and Etna [36] volcanoes. In the case of Mt. Etna, some authors reported that the south-eastern flank of this volcano slides into the Ionian Sea at a rates of centimetres per year. These results are based on the data of seafloor displacement collected during a 2016–2017 monitoring campaign [37].

In this paper, we analyse the background seismic signal recorded by NEMO-SN1 to determine the possible use of this signal in the volcano monitoring of Mt. Etna. Most amplitude increases of the background seismic signal are related to oceanographic processes. In the Western Ionian Sea, the influence of oceanographic dynamics on the background seismic signal is evident when comparing seismic data and wave heights recorded at a buoy located off Catania city harbour [38]. Due to their close correspondence, the gravity waves induced by local winds can be considered the main cause of oceanographic noise generation.

During the deployment of NEMO-SN1 seafloor observatory, a vigorous explosive event occurred on Mt. Etna, generating the powerful 2002–2003 eruption. Analysing the background seismic signal recorded by NEMO-SN1, we noted that some amplitude increases and frequencies are linked to Mt. Etna's activity, and that this signal has the same characteristics of the volcanic tremor recorded by land seismometers. We performed continuous monitoring of the eruptive activity of Mt. Etna from the seafloor, which is an unusual point of view. Some important evidence showed that the oceanographic noise was recorded clearly when Mt. Etna explosive activity was absent. Instead, oceanographic dynamics are hidden when explosive activity occurred (mainly as Strombolian explosions or lava fountains). Recognizing that the volcanic and oceanographic dynamic processes coexist may help to better comprehend the behaviour of Mt. Etna during its explosive activity, offering us the opportunity to study the submerged flank of the Mt. Etna volcano and to monitor its volcanic activity.

2. The NEMO-SN1 Seafloor Observatory

The NEMO-SN1 seafloor observatory was deployed in the Western Ionian Sea, about 40 km from Mt. Etna volcano, at a depth of 2100 m (Figure 1).

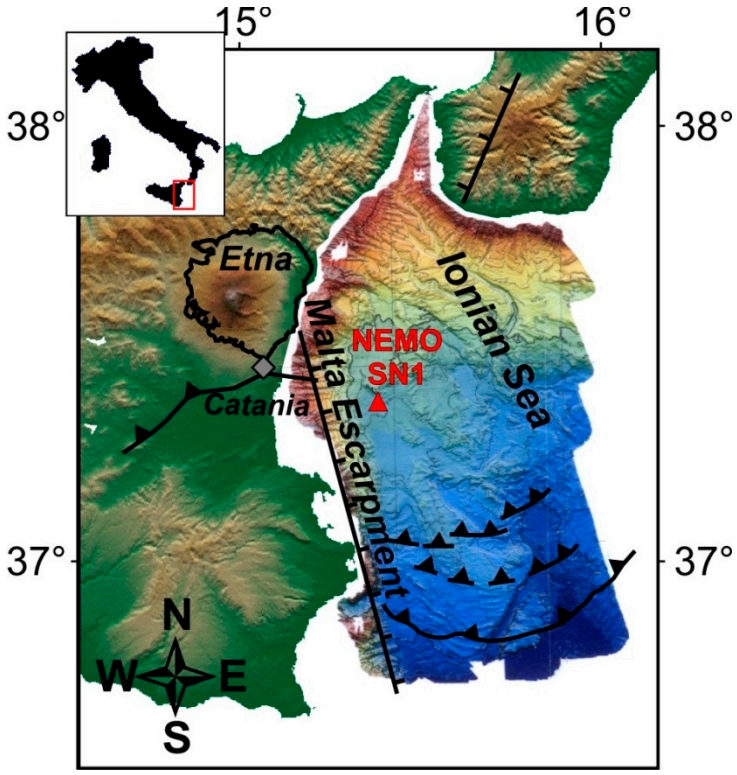

Figure 1. Western Ionian Sea multibeam map (redrawn from Marani et al. [39]). The red triangle indicates the location of the NEMO-SN1 seafloor observatory. Simplified geological structures are also reported (data obtained from previous studies [39–41]), where continuous lines with ticks refer to extensional and strike-slip faults, and lines with black triangles are thrusts and reverse faults (modified from Sgroi et al. [36]).

During the first experiment, NEMO-SN1 was deployed in stand-alone mode and operated continuously with an acoustic link for over 7 months (October 2002-May 2003 [15,16]). We analysed continuous background seismic data from October 17, 2002 to February 10, 2003.

The seismic data were recorded by a 3-component broadband seismometer (Guralp CMG-1T, Guralp Systems Ltd.-UK; 0.0027 to 50 Hz bandwidth and 100 Hz sampling rate), and synchronized by a high-precision rubidium clock (drift~0.5 ms/day) [13,42,43]. Seismological recordings were high quality due to both the installation procedure and the good ground coupling of the seismometer [44].

3. The 2002-2003 Mt. Etna Eruption

During the deployment of NEMO-SN1, a flank eruption occurred on Mt. Etna. The eruption was characterized by moderate lava emission, intense explosive activity, and abundant ash emission. The eruption started on October 26, 2002, two hours after the occurrence of a seismic crisis [45,46], with fissures opening on the NE and S flanks [47]. NEMO-SN1, besides the recording the volcano-tectonic earthquakes that preceded the onset of the eruption, recorded several dozens of earthquakes associated with the seismic crisis, but these were not well recorded and located by the permanent seismic network on the volcano edifice [16].

Magma accumulation, followed by ascent of magma and depressurization of the edifice due to the eastern flank spreading, triggered the eruption [47,48]. The eruption was associated with strong ground deformation at different times and for different durations [49].

A concise description of the 2002–2003 Mt. Etna volcanic activity is reported in Table 1 (modified from Andronico et al. [47] and Carbone et al. [50]).

Table 1. Chronology of the volcanic activity during the 2002–2003 Mt. Etna eruption (modified from previous studies [47,50]). Numbers 1 to 5 are the sub-periods of different volcanic activity compared to the increases in background seismic signal amplitudes shown in Figures 2a and 4a.

	Period	Date	Chronology of the Volcanic Activity
1	pre-eruption	15–25 October 2002	Degassing activity occasionally accompanied by ash emissions
2	eruption onset	26 October 2002 27 October 2002 28–30 October 2002 31 October 2002	At 20:12 UTC an intense earthquake swarm marks the onset of the 2002-2003 Etna eruption Strong Strombolian activity on the north-eastern flank Intense fire fountain activity on the southern flank End of the effusive activity on the southern flank Persistence of the explosive activity
3	Eruption (explosive activity)	1–11 November 2002 12–14 November 2002 15–21 November 2002	Intense fire fountain activity on the southern flank Intermittent Strombolian activity Alternation of Strombolian activity and lava fountain episode
4	Eruption (explosive and effusive activity)	22 November 2002 23–25 November 2002 26–27 November 2002 28–30 November 2002 1–10 December 2002 11–31 December 2002	Effusive activity Middle-high explosive activity Fountaining activity Strong jets and ash emission of explosive vent Explosive activity on the southern flank Effusive and explosive activity with variable intensity on the south-eastern flank
5	end of eruption	1–27 January 2003 28 January 2003	Progressive decrease of the frequency and intensity of explosive activity End of eruptive activity

4. Background Seismic Signals from NEMO-SN1

We computed the RMS (Root Mean Square) amplitude of the seismic signal (Z component) recorded by NEMO-SN1 to discriminate the contributions of the sea dynamics and volcanic activity of Mt. Etna. We reconstructed the time pattern of the background seismic signal filtering in two frequency bands: the first ranging between 0.1 and 5 Hz (Figure 2a), and the second between 0.5 and 5 Hz (Figure 4a). The signals in these two frequency bands appeared very differently. Figure 2a shows the signal filtered in 0.1–5 Hz and shows several background increases with high amplitudes that lasted several days.

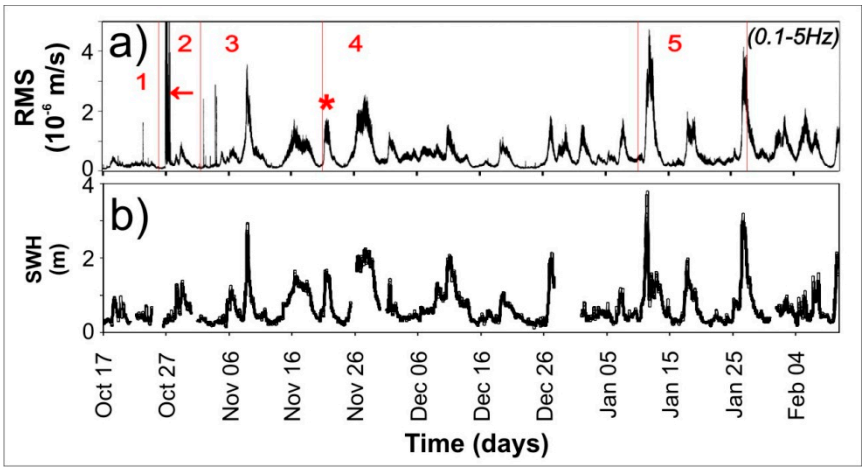

Figure 2. Comparison between (**a**) RMS of background seismic signal (filtered in the range of 0.1 to 5 Hz) and (**b**) significant Sea Wave Height (SWH). Red vertical bars and numbers refer to the period of volcanic activity described in Table 1; the red arrow indicates the 2002–2003 eruption onset; the red asterisk marks the episode of oceanographic noise increase analysed in Figure 3b.

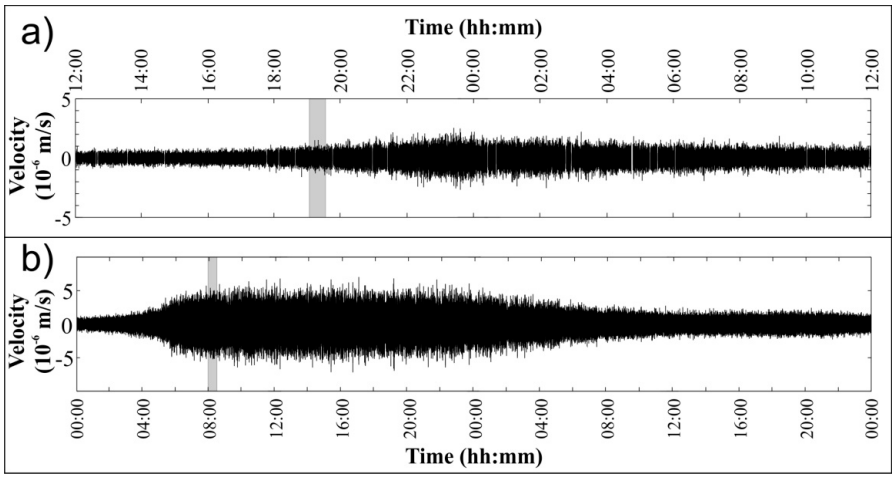

Figure 3. (**a**) Vertical component of background seismic signal (from November 4, 2002, 12:00 p.m. to November 5, 12:00 p.m.). The amplitude increase was recorded during a lava fountain episode. Due to the close correspondence between the background seismic signal and the volcanic activity, we indicated this signal as a volcanic tremor. (**b**) Vertical component of background seismic signal (from November 21, 12:00 a.m. to November 23, 12:00 a.m.). This background seismic increase was not associated with volcanic activity, so we labelled this signal oceanographic noise.

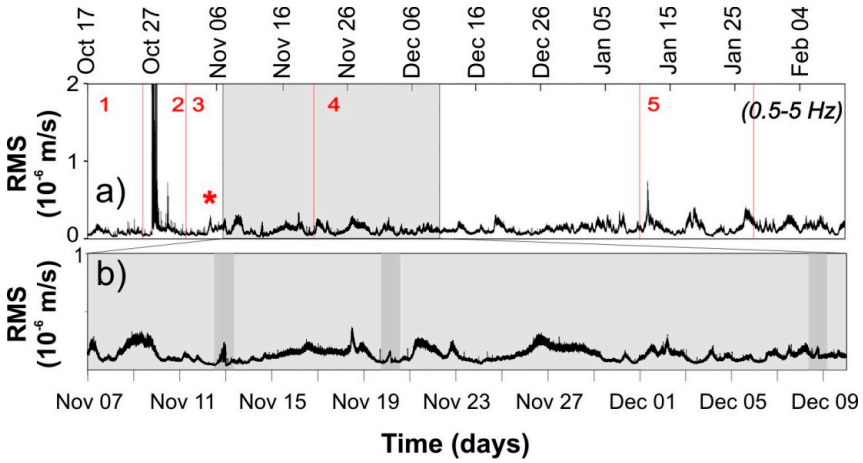

Figure 4. (**a**) RMS computed on the background seismic signal filtered within 0.5–5 Hz. Vertical bars and numbers refer to the period of volcanic activity described in Table 1. The light grey rectangular area marks the time series zoomed in Figure 4b; the red asterisk represents the background signal increases associated with the volcanic tremor shown in Figure 3a. (**b**) Time series zoomed in the period of November 7 to December 10, 2002. Three increases of tremor amplitude (highlighted with grey stripes) occurred during two lava fountains and the opening of new effusive vents [47,50].

These increases were not correlated with the explosive activity of Mt. Etna but were related to the sea dynamics. Figure 2b shows the Sea Wave Height (SWH) recorded at the buoy located off Catania harbour [38]. A correlation between the occurrence of these noise increases associated with SWH data is observed. This highlights that the noise is mainly associated with the local sea wave conditions affecting the seismological signal in the microseismic band (0.1–0.5 Hz; [25]).

In Figure 4a, we reconstructed the time pattern of the background seismic signal filtered in the frequency range between 0.5 and 5 Hz, as tremors mainly reflect the volcanic activity in this range [31]. The correspondence between the beginning and evolution of the explosive activity and the pattern of the background seismic signal recorded by NEMO-SN1 (Figure 4a) was checked using reports describing the volcanic activity [51].

The increases in background signal are strongly linked to the explosive activity of Mt. Etna: the highest amplitudes were visible during the eruption onset (27 October 2002), whereas slight amplitude increases were only visible during the occurrence of lava fountains and fracture opening episodes, corresponding to the main phases of volcanic activity (Table 1). These increases in the background signal showed evident similarities with the low-frequency signal identified as volcanic tremor, typically observed on land; in the time period of November 7 to December 9 (Figure 4b), two lava fountain episodes and the opening of new effusive vents occurred, accompanied by effusive and Strombolian activity [47,50].

5. Time, Spectral, and Polarization Analyses

Time, spectral, polarization, and particle-motion analyses were performed on continuous seismic signals to characterize volcanic tremors and oceanographic noise. In particular, we compared two episodes of continuous signal amplitude increase to discriminate between the source of the two signals. The continuous Z-component signals shown in Figure 3a,b were 0.1–5 Hz filtered. A background signal increase was recorded simultaneously with the occurrence of a lava fountain episode (4–5 November 2002; Figure 3a). Other increases in the background seismic signal were not associated with explosive activity. One of these episodes (Figure 3b) occurred on 21–22 November 2002.

The amplitude trends of both signals are rather similar (Figure 3a,b), except for the roughly higher values of oceanographic noise amplitude.

In order to estimate the quantitative relationship between SWH and RMS computed in both the 0.1–5 Hz and the 0.5–5 Hz frequency band, we performed a cross-correlation analysis between the two signals. We considered the two episodes represented in Figure 3 as well as the whole period shown in Figure 2a,b (Figure 5).

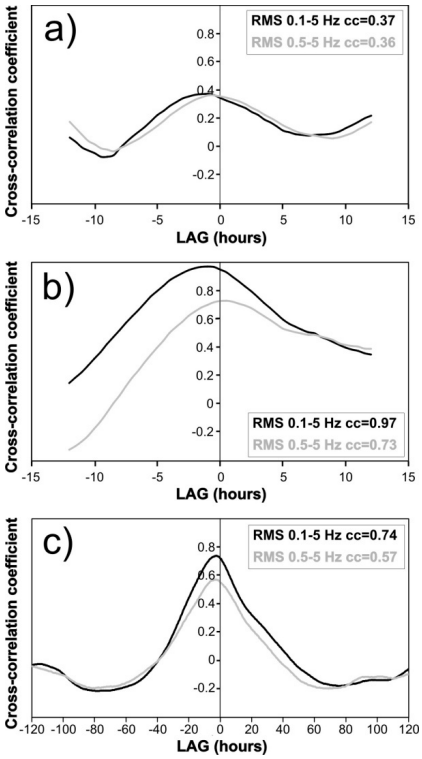

Figure 5. Cross-correlation computed between the RMS 0.1–5 Hz filtered and SWH (black line) and the RMS 0.5–5 Hz filtered and SWH (grey line) on (**a**) volcanic tremor (November 4–5, 2002 in Figure 3a), (**b**) oceanographic noise (November 21–22 in Figure 3b) and (**c**) the whole period (November 1, 2002–February 10, 2003). The cc values in the rectangular area represent the correlation coefficient. The lags are negative when seismic RMS follows SWH time series.

The results show that the correlation between volcanic tremor and SWH is very poor, in particular for the seismic signal filtered in the 0.1–5 Hz frequency band [25] (cc = 0.37; Figure 5a). On the other hand, a very high correlation between oceanographic noise and SWH is found (correlation coefficients cc = 0.97 and cc = 0.73 for 0.1–5 Hz and 0.5–5 Hz, respectively; see Figure 5b). Such findings suggest that the oceanographic noise recorded by NEMO-SN1 is probably due to gravity waves generated on the air-sea interface.

With the aim of supporting these results, a cross-correlation analysis was performed on the whole period (Figure 5c). We started the cross-correlation analysis on November 1, 2002, excluding the peak linked to the seismic swarm that preceded and accompanied the eruption onset. The cross-correlation confirms a higher value for the RMS computed in the 0.1–5 Hz band (cc = 0.74) compared to the one in the 0.5–5 Hz band (cc = 0.57). This indicates that the seismic signal recorded by NEMO-SN1 mainly consists of oceanographic noise, well detected in the 0.1–0.5 Hz frequency band [25]. Further, the results suggest that the local wind could be the main source in oceanographic noise generation.

The spectrogram and spectra (Figure 6a,c and Figure 6b,d, respectively) computed on the two signals are different mainly in the 0.01–0.5 Hz frequency band. To better appreciate the spectral difference between volcanic tremor and oceanographic noise, we compared spectrograms computed on the two signals related to the lava fountain episode and a background signal increase (Figure 6a,c), both calculated in a 30-minute time window (grey striped in Figure 3a,b). We observed that the volcanic tremor (Figure 6a) was characterized by a variable spectral amplitude content in the 0.1–0.5 Hz frequency band, whereas oceanographic noise (Figure 6c) had one well-defined near-monochromatic frequency around 0.3 Hz.

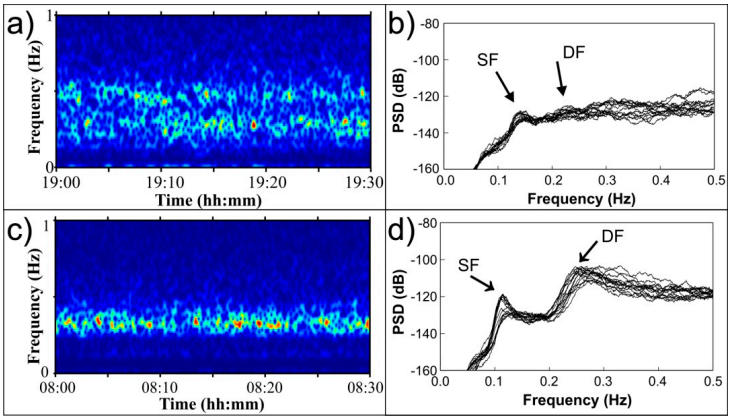

Figure 6. (**a**) Spectrogram for a 30-minute time window (vertical grey stripe in Figure 3a) for volcanic tremor recorded between 7:00 and 7:30 p.m. GMT during a lava fountain episode. Red, yellow, and green colours define the dominant spectral amplitudes; light to dark blue colours define lower amplitudes and background. The spectrogram shows a variable low-frequency content in the 0.1–1 Hz frequency band. (**b**) Power Spectral Density (PSD) computed for 14 30-minute segments (Z component of the seismometer), zoomed in on the frequency band 0–0.5 Hz. Single Frequency (SF) and Double Frequency (DF) peaks are not evident. (**c**) Spectrogram for a 30-minute time window (vertical grey stripe in Figure 3b) for oceanographic noise recorded between 8:00 and 8:30 a.m. GMT. A near-monochromatic frequency around 0.3 Hz is visible; it is consistent with the DF peak. (**d**) PSD computed on 14 30-minute segments (Z component of the seismometer), zoomed in on the frequency band 0–0.5 Hz. The two frequency peaks related to microseisms (~0.1 and ~0.3 Hz) are visible.

A more detailed spectral analysis of both oceanographic noise and volcanic tremor signals was performed on the 0.0–0.5 Hz frequency band (Figure 6b,d) on 14 30-minute segments. The volcanic tremor showed a rough frequency peak close to 0.1 Hz, whereas spectral amplitudes remained almost constant at frequencies ranging between 0.2 and 0.5 Hz (Figure 6b). Spectra computed on oceanographic noise (Figure 6d) show the two peaks at frequencies close to 0.1 and 0.3 Hz. These frequencies correspond to

the two typical microseismic peaks caused by ocean wave energy coupling into the motion of the earth: the Single Frequency (SF) peak (~0.1 Hz) and the much stronger Double Frequency (DF) peak (~0.3 Hz) [25]. The SF peak is generated by direct ocean wave pressure fluctuations at the ocean bottom; the amplitude of wave-induced pressure fluctuations decreases exponentially with depth from the sea surface depending on the bathymetry. The DF peak is produced by the interaction of sea gravity waves with the seafloor [19,25]. The SF peak has been associated with high-amplitude storm waves impacting long stretches of coastline nearly simultaneously, whereas the DF peak is related to wind speed and direction, implying that the energy reaching the ocean floor is generated locally by ocean gravity waves [52]. In the Ionian Sea, the SF peak is considered characteristic of deep-sea monitoring sites that are not too far from the coastlines, which is more easily observed during favourable weather conditions. The presence of the energetic DF peak suggests the influence of local winds [53]. Although spectra of oceanographic noise showed well-defined SF and DF peaks (Figure 6d), in the volcanic tremor signal spectra, the SF peaks are not clearly delineated (Figure 6b). The spectral amplitudes of SF and DF peaks computed for the volcanic tremor signal were both about −130 dB, whereas the SF and DF peaks of oceanographic noise signal had more pronounced spectral amplitudes (about −120 dB and −90 dB, respectively). This means that spectral amplitudes linked to volcanic activity hide the effects linked to the sea in this low-frequency band.

Due to the availability of continuous broadband three-component signals, we performed polarization and particle-motion analyses with the aim of identifying the direction of the locations of the sources. We used the standard covariance matrix method [54,55], which works in the time domain by bandpass filtering the signal around the frequency band of interest. The broadband data from the different components were converted to ground velocity by deconvolving the instrument response. We computed the polarization on the three-component signals by applying the Covariance Matrix Decomposition (CMD) developed in the SEISMPOL code [56].

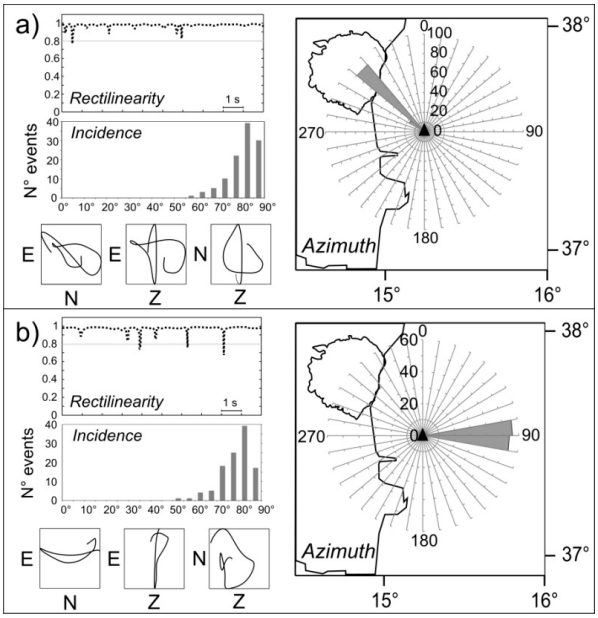

Figure 7. Polarization and particle motion computed on amplitude increases associated with: (**a**) volcanic tremor and (**b**) oceanographic noise. Examples of rectilinearity, incidence, and azimuth values computed on a 10-s-long window of 0.1–2 Hz-filtered signal; hodograms of particle motion were computed on a 4-s-long window. A total of 110 windows for both volcanic tremor and oceanographic noise were analysed. Polarization and particle motion show high values of rectilinearity (> 0.8) and high incidence angles (> 60°), typical converted phases from P-waves to S-waves (P-to-S) at the seafloor boundary in both signals. The azimuth values reported in the two rose diagram show that the volcanic tremor propagated from NW to SE, compatible with a wave front coming from Mt. Etna; oceanographic noise shows a constant E–W direction roughly perpendicular to the coast and consistent with the sea wave direction of propagation.

The background seismic signal recorded by NEMO-SN1 has a complex waveform, where different aspects act concurrently with the polarization of a signal in the same frequency band. We attempted polarization analyses using a total of 110 10-s-long windows of 0.1–2 Hz-filtered signal. The results from polarization were compared with those derived from particle motion analysis, performed using 110 4-s-long windows of 0.1–2 Hz filtered signal. Polarization and particle motion computed on volcanic tremor and oceanographic noise showed high values of rectilinearity (>0.8) and high incidence angles (>60°) (Figure 7b). Results from these analyses indicate that most energy in the 0.1–2 Hz frequency band is due to the generation of converted waves prevalently from P–waves to S–waves (P-to-SV) at the seafloor boundary for both signals. Our results concur with those of Imanishi et al. [57], who found that low-frequency noise is composed of nearly vertical incident S-waves. In the case of volcanic tremors, our results agree with those recorded at Mt. Etna and other volcanic areas. A wavefield consisting of P-waves radiated by a vertical extended source was observed at Mt. Etna [58,59]; body waves radiated by an extended source characterized the wavefield recorded some kilometres away from the summit craters. Dominant P-SV converted waves have been identified in the Phlegrean Caldera [60], whereas S-waves were identified as the dominant wave type at Arenal volcano [61].

The most relevant difference between volcanic tremor and oceanographic noise is observed in the strong directivity of wave propagation, shown in the two rose diagrams in Figure 7a,b. Volcanic tremor propagates from NW to SE, compatible with a wave front coming from Mt. Etna, with azimuth values ranging from 290° to 320° (Figure 7a). The particle motion of oceanographic noise (Figure 7b) shows an E–W direction, corresponding to the sea wave direction perpendicular to the coast (azimuth ranging 85–94°).

6. Comparison between Volcanic Tremor and Oceanographic Noise

We computed the Power Spectral Density (PSD) by applying Fast Fourier Transform to characterize the background seismic signal. Figure 8a–d show the PSD computed over two-hour-long segments chosen in four different periods: (1) October 17 refers to the non-eruptive period preceding the eruption onset, (2) October 27 coincides with the eruption onset, (3) November 22 corresponds to a background seismic increase not associated with explosive activity, and (4) December 8 is the eruptive period.

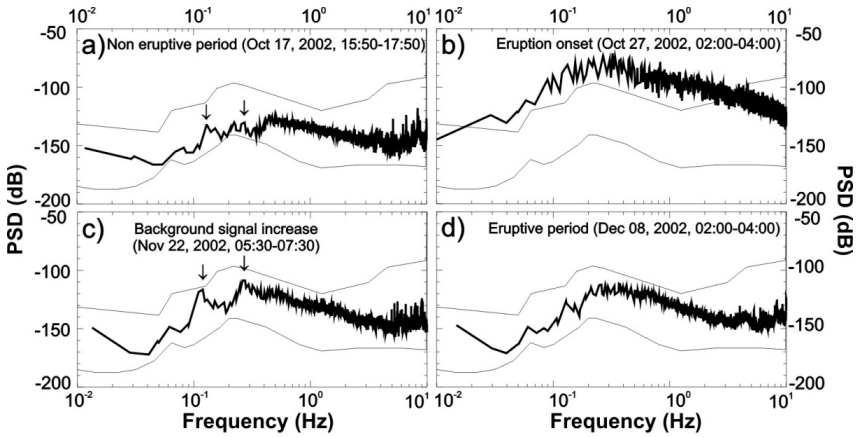

Figure 8. Two-hour-long PSD computed on seismic data. Four different intervals were analysed: (**a**) non-eruptive period (October 17, 2002), (**b**) the eruption onset (October 27, 2002), (**c**) background signal increase not correlated with volcanic activity (November 22, 2002), and (**d**) the eruptive period (December 8, 2002). The two black lines represent the Peterson's reference models [62]. (**b**) Seismic data show the maximum energy content in correspondence of the eruption onset, where the spectral amplitudes exceed the reference model. (**d**) Spectrum computed on the eruptive period is similar in frequency to the previous period but shows lower energy. Their patterns are representative of the volcanic activity. (**a**) The non-eruptive period and (**c**) the background signal increase show a different trend with two microseismic spectral peaks at ~0.1 and ~0.3 Hz, respectively (indicated with black arrows), associated with sea dynamics.

The comparison of the computed spectra with the reference Low-Noise Model (LNM) and High-Noise Model (HNM) curves [62] shows that during the eruption onset (Figure 8b), the spectral amplitude exceeded the HNM curves, being about 40 dB higher than the PSD computed in the eruptive period (Figure 8d). Both spectra show that the energy of the seismic data is concentrated in the 0.1–4 Hz frequency band, with a higher energy content in the 0.5–2 Hz frequency band (Figure 8b), which was typical of the Mt. Etna volcanic tremor during the occurrence of the 13 lava fountains in 2013 [36]. The non-eruptive period (Figure 8a) and the background seismic increase period (Figure 8c) show a different pattern, with the presence of two peaks in the typical microseismic band: the SF peak (~0.1 Hz) and the stronger DF peak (~0.3 Hz) [25]. In Figure 8a,c, the pattern of microseismic spectra in the 0.01-0.5 Hz band shows the typical spectral features of deep water, as in the Cascadian area [26].

7. Discussion and Conclusions

The typical background seismic signal recorded by seafloor stations is a continuous oceanographic noise that is associated with tidal variation and currents and is due to ocean loading, which causes local crustal stresses [27]. In order to focus on the possible generation of oceanographic noise in the Ionian Sea, we computed the RMS amplitude pattern of the seismic signal filtered in the frequency range between 0.1 and 5 Hz, and compared it with the wave height recorded at the buoy located off Catania harbour [38] (Figure 2b). The frequency of oceanographic noise recorded by NEMO-SN1 is primarily below 0.5 Hz and we found two distinctive peaks at ~0.1 and ~0.3 Hz (SF and DF microseismic peaks, respectively) in the spectrum of the oceanographic noise signal (Figure 6d). The sea gravity waves induced by local winds are the main cause of the oceanographic noise generation.

In October 2002, a vigorous eruptive and explosive event started on Mt. Etna. The eruption provided an occasion to test the capacity of NEMO-SN1 to record the low-frequency seismic signals associated with volcanic activity (volcanic tremor) and to discriminate the low-frequency signals from those associated with sea dynamics (oceanographic noise). During the eruption, we observed a strict correspondence between amplitude increases of the background seismic signal recorded at NEMO-SN1 and the occurrence of explosive activity (Figures 4 and 3a). Spectral analysis performed on the background seismic signal demonstrated a frequency range between 0.1 and 4 Hz, with higher energy in the 0.5-2 Hz frequency band (Figure 8b), which is comparable to the predominant frequencies closer to 2 Hz recorded by land stations located on Mt. Etna [34,63] and by ocean bottom seismometers (OBSs) located close to Etna and Stromboli volcanoes [35,36]. Changes in spectral amplitudes during the two different phases of the eruption (from about –60 dB to –120 dB in Figure 8b,d) depend on the intensity of volcanic activity [34], but also on the tremor source position [63].

The cross-correlation analysis between the seismic signal (RMS) recorded by NEMO-SN1 and the SWH suggests that the oceanographic noise probably originated from local winds perturbing the sea surface. Such noise dominates the seismic signal over the whole studied period and it is mainly concentrated in the 0.1-5 Hz frequency band [25]. On the other hand, the seismic signal generated by the volcano (volcanic tremor) highlights a very low correlation with the SWH and, accordingly, with the oceanographic noise. Consequently, the cross-correlation analysis between RMS and SWH allowed us to effectively discriminate the volcanic tremor from the oceanographic noise.

The wave field compositions resulting from polarization and particle motion analyses computed for volcanic tremor and oceanographic noise are rather similar, showing a complex overlapping pattern that consists mainly of converted waves (mainly P to SV waves). A source mechanism linked to pressure variations due to fluid movements is the driving force for both volcanic tremor and oceanographic noise generation. In the case of volcanic tremor, this mechanism is compatible with the presence of a storage zone for Mt. Etna that extends under the seafloor, linked to the dynamics of the magmatic fluids [64–68]. A compressive mechanism linked to pressure variations may explain the wave field composition of oceanographic noise. We inferred that oceanographic noise is largely due to the pressure applied by the sea gravity waves on the seafloor, which deform the underlying sediment and crust.

The most important difference between volcanic tremor and oceanographic noise is the strong directivity of the two signals. Volcanic tremors show a preferential direction from NW to SE (Figure 7a). This confirms that the 0.5–2 Hz bandpass filtered signals come directly from Mt. Etna. The oceanographic noise shows a marked directivity from polarization and particle motion analyses, having a predominant wave direction from E to W (rose diagram with a narrow range of azimuth values ranging from 85° to 94° in Figure 7b) and corresponding to the sea wave direction roughly perpendicular to the coast.

The spectra computed on volcanic signals recorded during the occurrence of explosive activity of Mt. Etna and non-eruptive periods provide meaningful results. Seismic data show the maximum energy corresponding to the eruption onset and eruptive period when their patterns are representative of the volcanic activity. During the non-eruptive period, increases in background signal are observed but spectra have a different trend with two visible microseismic spectral peaks at ~0.1 and ~0.3 Hz (Figure 8a,c, respectively) associated with the sea dynamics.

In the absence of explosive activity at Mt. Etna, sea dynamics prevail. When explosive activity increases, the energy associated with the volcanic tremor linked to Mt. Etna volcanism becomes the main contribution, prevailing on the oceanographic dynamics. Since volcanic tremors, as recorded by land seismic stations around Mt. Etna, were also observed on the seafloor, we inferred that explosive activity is generated by processes that are efficiently detected by the seafloor station.

The monitoring of the volcanic activity from a seafloor observatory can help to pinpoint possible hazard sources in the Western Ionian Sea. Understanding the similarities and differences of seismic signals containing the contribution of both volcanic and oceanographic processes may help assessing the behaviour during explosive activity at Mt. Etna, which is crucial to minimizing volcanic hazards.

Author Contributions: P.F. conceived and designed the field experiments; T.S. and G.D.G. analysed the data and contributed to the interpretation of the results; T.S. contributed to the writing of the manuscript and figure preparation. All authors participated in discussions of the results.

Funding: This research was funded by European Commission grant number 283465.

Acknowledgments: The authors thank Hitoshi Mikada and Valerio Iafolla for their valuable comments. We are indebted to the Assistant Editor Richard Li and the two anonymous reviewers for the fruitful revision of the paper and suggestions.

Conflicts of Interest: The authors declare no conflict of interest.

References

1. Favali, P.; Person, R.; Barnes, C.R.; Kaneda, Y.; Delaney, J.R.; Hsu, S.-K. Seafloor Observatory Science. In Proceedings of the OceanObs'09: Sustained Ocean Observations and Information for Society conference 2.2010, Venice, Italy, 21–25 September 2009; Hall, J., Harrison, D.E., Stammer, D., Eds.; ESA Publication: Venice, Italy, 2010. WPP-306.
2. Favali, P.; Beranzoli, L.; De Santis, A. (Eds.) *Seafloor Observatories: A New Vision of the Earth from the Abyss. Springer-Praxis Books in Geophysical Sciences*; Springer: Berlin/Heidelberg, Germany, 2015; 676p, ISBN 978-3-642-11373-4. e-ISBN 978-3-642-11374-1. [CrossRef]
3. Butler, R.; Chave, A.D.; Duennebier, F.K.; Yoerger, D.R.; Petitt, R.; Harris, D.; Wooding, F.B.; Bowen, A.D.; Bailey, J.; Jolly, J.; et al. Hawaii-2 Observatory pioneers opportunities for remote instrumentation in ocean studies. *Eos Trans. AGU* **2000**, *81*, 161–163. [CrossRef]
4. Caplan-Auerbach, J.; Duennebier, F.K. Seismic and acoustic signals detected at Lo'ihi Seamount by the Hawaii Undersea Geo-Observatory. *Geochem. Geophys. Geosys.* **2001**, *2*. [CrossRef]
5. ONC-Ocean Networks Canada. Available online: www.oceannetworks.ca (accessed on 20 December 2018).
6. Fox, C.G.; Dziak, R.P.; Matsumoto, H.; Schreiner, A.E. Potential for monitoring low level seismicity on the Juan de Fuca Ridge using military hydrophone arrays. *Mar. Technol. Soc. J.* **1994**, *27*, 22–30.
7. Dziak, R.P.; Hammond, S.R.; Fox, C.G. A 20-year hydroacoustic time series of seismic and volcanic events in the Northeast Pacific Ocean. *Oceanography* **2011**, *24*, 280–293. [CrossRef]

8. OOI-Ocean Observatories Initiative. Available online: https://oceanobservatories.org/ (accessed on 18 September 2018).
9. Tolstoy, M.; Wilcock, W.S.D.; Tan, Y.J.; Waldhauser, F. A tale of two eruptions: How data from Axial Seamount led to a discovery on the East Pacific Rise. *Oceanography* **2018**, *31*, 124–125. [CrossRef]
10. Wilcock, W.S.D.; Dziak, R.P.; Tolstoy, M.; Chadwick, W.W., Jr.; Nooner, S.L.; Bohnenstiehl, D.R.; Caplan-Auerbach, J.; Waldhauser, F.; Arnulf, A.F.; Baillard, C.; et al. The recent volcanic history of Axial Seamount: Geophysical insights into past eruption dynamics with an eye toward enhanced observations of future eruptions. *Oceanography* **2018**, *31*, 114–123. [CrossRef]
11. Tréhu, A.M.; Wilcock, W.S.D.; Hilmo, R.; Bodin, P.; Connolly, J.; Roland, E.C.; Braunmiller, J. The role of the Ocean Observatories Initiative in monitoring the offshore earthquake activity of the Cascadia subduction zone. *Oceanography* **2018**, *31*, 104–113. [CrossRef]
12. EMSO ERIC-European Multidisciplinary Seafloor and Water-Column Observatory European Research Infrastructure Consortium. Available online: www.emso.eu (accessed on 24 October 2017).
13. Favali, P.; Beranzoli, L.; D'Anna, G.; Gasparoni, F.; Gerber, H.W. NEMO-SN1 The 1st real-time seafloor observatory of ESONET. *Nucl. Instrum. Methods Phys. Res. Sect. A* **2006**, *567*, 462–467. [CrossRef]
14. Favali, P.; Beranzoli, L.; Italiano, F.; Migneco, E.; Musumeci, M.; Papaleo, R. NEMO-SN1 observatory developments in view of the European Research Infrastructures EMSO and KM3NET. *Nucl. Instrum. Methods Phys. Res. Sect. A* **2011**, *626–627*, S53–S56. [CrossRef]
15. Favali, P.; Chierici, F.; Marinaro, G.; Giovanetti, G.; Azzarone, A.; Beranzoli, L.; De Santis, A.; Embriaco, D.; Monna, S.; Lo Bue, N.; et al. NEMO-SN1 Abyssal Cabled Observatory in the Western Ionian Sea. *IEEE J. Ocean. Eng.* **2013**, *38*, 358–374. [CrossRef]
16. Sgroi, T.; Beranzoli, L.; Di Grazia, G.; Ursino, A.; Favali, P. New observations of local seismicity by the SN-1 seafloor observatory in the Ionian Sea, off-shore eastern Sicily (Italy). *Geophys. J. Int.* **2007**, *169*, 490–501. [CrossRef]
17. Monna, S.; Sgroi, T.; Dahm, T. New insights on volcanic and tectonic structures of the southern Tyrrhenian (Italy) from marine and land seismic data. *Geochem. Geophys. Geosys.* **2013**, *14*, 3703–3719. [CrossRef]
18. Hasselmann, K. A statistical analysis of the generation of Microseisms. *Rev. Geophys.* **1963**, *1*, 177–209. [CrossRef]
19. Webb, S.C. Seismic noise on land and on the seafloor. *Int. Geophys. Ser.* **2002**, *81*, 305–318.
20. Dahm, T.; Tilmann, F.; Morgan, J.P. Seismic broadband ocean bottom data and noise observed with free-fall stations: Experiences from long-term deployments in the North Atlantic and the Tyrrhenian Sea. *Bull. Seismol. Soc. Am.* **2006**, *96*, 647–664. [CrossRef]
21. Vassallo, M.; Bobbio, A.; Iannaccone, G. A comparison of seafloor and on-land seismic ambient noise in the Campi Flegrei Caldera, southern Italy. *Bull. Seismol. Soc. Am.* **2008**, *98*, 2962–2974. [CrossRef]
22. Stephen, R.A.; Spiess, F.N.; Collins, J.A.; Hildebrand, J.A.; Orcutt, J.A.; Peal, K.R.; Vernon, F.L.; Wooding, F.B. Ocean seismic network pilot experiment. *Geochem. Geophys. Geosyst.* **2003**, *4*. [CrossRef]
23. Delyander, P.S.; Butman, B.; Sherwood, C.R.; Signell, R.P.; Wilkin, J.L. Characterizing wave- and current-induced bottom shear stress: US middle Atlantic continental shelf. *Cont. Shelf Res.* **2013**, *52*, 73–86. [CrossRef]
24. Wilcock, W.S.D. Tidal triggering of microearthquakes on the Juan de Fuca Ridge. *Geophys. Res. Lett.* **2001**, *28*, 3999–4002. [CrossRef]
25. Webb, S.C. Broadband seismology and noise under the ocean. *Rev. Geophys.* **1998**, *36*, 105–142. [CrossRef]
26. Toomey, D.R.; Allen, R.; Barclay, A.H.; Bell, S.W.; Bromirski, P.; Carlson, R.L.; Chen, X.; Collins, J.A.; Dziak, R.P.; Evers, B.; et al. The Cascadia initiative: A sea change in seismological studies of subduction zones. *Oceanography* **2014**, *27*, 138–150. [CrossRef]
27. Tolstoy, M.; Vernon, F.L.; Orcutt, J.A.; Wyatt, F.K. Breathing of the seafloor: Tidal correlations of seismicity at Axial volcano. *Geology* **2002**, *30*, 503–506. [CrossRef]
28. Buskirk, R.E.; Frohlich, C.; Latham, G.V.; Chen, A.T.; Lawton, J. Evidence that biological activity affects ocean bottom seismograph recordings. *Mar. Geophys. Res.* **1981**, *5*, 189–205.
29. Tréhu, A.M. Coupling of ocean bottom seismometers to sediment: Results of tests with the US Geological Survey ocean bottom seismometer. *Bull. Seism. Soc. Am.* **1985**, *75*, 271–289.

30. Bécel, A.; Diaz, J.; Laigle, M.; Hirn, A.; TTWRCR Group. Searching for unconventional seismic signals on a subduction zone with a submerged forearc: OBS offshore the Lesser Antilles. *Tectonophysics* **2013**, *603*, 21–31. [CrossRef]
31. Chouet, B. Long-Period volcano seismicity: Its source and use in eruption forecasting. *Nature* **1996**, *380*, 309–316. [CrossRef]
32. Alparone, S.; Andronico, D.; Lodato, L.; Sgroi, T. Relationship between tremor and volcanic activity during the Southeast Crater eruption on Mount Etna in early 2000. *J. Geophys. Res.* **2003**, *108*, 2241. [CrossRef]
33. Privitera, E.; Sgroi, T.; Gresta, S. Statistical analysis of intermittent volcanic tremor associated with the September 1989 summit explosive eruptions at Mt. Etna, Sicily. *J. Volcanol. Geotherm. Res.* **2003**, *120*, 235–247. [CrossRef]
34. Falsaperla, S.; Alparone, S.; D'Amico, S.; di Grazia, G.; Ferrari, F.; Langer, H.; Sgroi, T.; Spampinato, S. Volcanic Tremor at Mt. Etna, Italy, Preceding and Accompanying the Eruption of July-August, 2001. *Pure Appl. Geophys.* **2005**, *162*, 2111–2132. [CrossRef]
35. Sgroi, T.; Montuori, C.; Agrusta, R.; Favali, P. Low-frequency seismic signals recorded by OBS at Stromboli volcano (Southern Tyrrhenian Sea). *Geophys. Res. Lett.* **2009**, *36*, L04305. [CrossRef]
36. Sgroi, T.; Monna, S.; Embriaco, D.; Giovanetti, G.; Marinaro, G.; Favali, P. Geo-hazards in the Western Ionian Sea: Insights from non-earthquake signals recorded by the NEMO-SN1 seafloor observatory. *Oceanography* **2014**, *27*, 154–166. [CrossRef]
37. Urlaub, M.; Petersen, F.; Gross, F.; Bonforte, A.; Puglisi, G.; Guglielmino, F.; Krastel, S.; Lamge, D.; Kopp, H. Gravitational collapse of Mount Etna's southeastern flank. *Sci. Adv.* **2018**, *4*, eaat9700. [CrossRef] [PubMed]
38. RON-Rete Ondametrica Nazionale. Available online: http://dati.isprambiente.it/accesso-ai-dati/download/ (accessed on 20 December 2018).
39. Marani, M.P.; Gamberi, F.; Bortoluzzi, G.; Carrara, G.; Ligi, M.; Penitenti, D. Seafloor bathymetry of the Ionian Sea. In *From Seafloor to Deep Mantle: Architecture of the Tyrrhenian Backarc Basin*; Marani, M.P., Gamberi, F., Bonatti, E., Eds.; Memorie Descrittive Carta Geologica d'Italia-SGI Società Geologica Italiana: Roma, Italy, 2004; Volume 44, Plate 3.
40. Meletti, C.; Patacca, E.; Scandone, P. Construction of a seismotectonic model: The case of Italy. *Pure Appl. Geophys.* **2000**, *157*, 11–35. [CrossRef]
41. Argnani, A.; Bonazzi, C. Malta Escarpment fault zone offshore eastern Sicily: Pliocene-Quaternary tectonic evolution based on new multichannel seismic data. *Tectonics* **2005**, *24*, TC4009. [CrossRef]
42. Favali, P.; Beranzoli, L.; D'Anna, G.; Gasparoni, F.; Marvaldi, J.; Clauss, G.; Gerber, H.W.; Nicot, M.; Marani, M.P.; Gamberi, F.; et al. A fleet of multiparameter observatories for geophysical and environmental monitoring at seafloor. *Ann. Geophys.* **2006**, *49*, 659–680.
43. Gasparoni, F.; Furlan, F.; Bruni, F.; Zanon, F.; Favali, P.; Beranzoli, L.; Marinaro, G.; De Santis, A.; Gerber, H.W. GEOSTAR-class observatories 1995–2012: A technical overview. In *Seafloor Observatories: A New Vision of the Earth from the Abyss*; Favali, P., Beranzoli, L., de Santis, A., Eds.; Springer-Praxis books in Geophysical Sciences; Springer: Berlin/Heidelberg, Germany, 2015; pp. 229–304. ISBN 978-3-642-11373-4. e-ISBN 978-3-642-11374-1. [CrossRef]
44. Monna, S.; Frugoni, F.; Montuori, C.; Beranzoli, L.; Favali, P. High quality seismological recordings from the SN-1 deep seafloor observatory in the Mt. Etna region. *Geophys. Res. Lett.* **2005**, *32*, L07303. [CrossRef]
45. Patanè, D. Aggiornamento delle Attività di Monitoraggio Sismico all'Etna. 2002. Available online: http://www.ct.ingv.it/report/Rapporto_eruzione20021030.pdf (accessed on 15 October 2015).
46. Allard, P.; Behncke, B.; D'Amico, S.; Neri, M.; Gambino, S. Mount Etna 1993–2005: Anatomy of an evolving eruptive cycle. *Earth Sci. Rev.* **2006**, *78*, 85–114. [CrossRef]
47. Andronico, D.; Branca, S.; Calvari, S.; Burton, M.R.; Caltabiano, T.; Corsaro, R.A.; Del Carlo, P.; Garfì, G.; Lodato, L.; Miraglia, L.; et al. A multi-disciplinary study of the 2002–03 Etna eruption: Insights for a complex plumbing system. *Bull. Volc.* **2005**, *67*, 314–330. [CrossRef]
48. Zhang, X.; Zhang, H. Wavelet-based time-dependent travel time tomography method and its application in imaging the Etna volcano in Italy. *J. Geophys. Res.* **2015**. [CrossRef]
49. Aloisi, M.; Bonaccorso, A.; Gambino, S.; Mattia, M.; Puglisi, G. Etna 2002 eruption imaged from continuous tilt and GPS data. *Geophys. Res. Lett.* **2003**, *30*, 2214. [CrossRef]
50. Carbone, D.; Zuccarello, L.; Saccorotti, G.; Greco, F. Analysis of simultaneous gravity and tremor anomalies observed during the 2002–2003 Etna eruption. *Earth Planet. Sci. Lett.* **2006**, *245*, 616–629. [CrossRef]

51. INGV—Istituto Nazionale di Geofisica e Vulcanologia. Ossevatorio Etneo. Available online: http://www.ct.ingv.it/it/banca-dati-delle-eruzioni/eruzioni-etna.html (accessed on 15 October 2015).
52. Bromirski, P.D.; Duennebier, F.K.; Stephen, R.A. Mid-ocean microseisms. *Geochem. Geophys. Geosys.* **2005**, *6*, Q04009. [CrossRef]
53. De Caro, M.; Monna, S.; Frugoni, F.; Beranzoli, L.; Favali, P. Seafloor seismic noise at Central Eastern Mediterranean sites. *Seismol. Res. Lett.* **2014**, *85*, 1019–1033. [CrossRef]
54. Montalbetti, J.F.; Kanasewich, K.R. Enhancement of teleseismic body phases with a polarisation filter. *Geophys. J. R. Astron. Soc.* **1970**, *21*, 119–129. [CrossRef]
55. Jurkevics, A. Polarisation analysis of three-component array data. *Bull. Seismol. Soc. Am.* **1988**, *78*, 1725–1743.
56. Patanè, D.; Ferrari, F. A Visual-Basic computer program for interactive and automatic earthquakes waveform analysis. *Comput. Geosci.* **1998**, *23*, 1005–1012. [CrossRef]
57. Imanishi, K.; Takeda, N.; Kuwahara, Y.; Hoshino, M.; Koizumi, N.; Ide, S. Wavefield and source spectra of non-volcanic low-frequency tremors in a southwest Japan subduction zone. In *American Geophysical Union, Fall Meeting*; American Geophysical Union: Washington, DC, USA, 2008; Abstract U33A-0031.
58. Ereditato, D.; Luongo, G. Volcanic tremor wave field during quiescent and eruptive activity at Mt. Etna (Sicily). *J. Volcanol. Geotherm. Res.* **1994**, *61*, 239–251. [CrossRef]
59. Wegler, U.; Seidl, D. Kinematic parameters of the tremor wave field at Mt. Etna (Sicily). *Geophys. Res. Lett.* **1997**, *24*, 759–762. [CrossRef]
60. Ferrucci, F.; Hirn, A.; De Natale, G.; Virieux, J.; Mirabile, L. P-SV Conversions at a shallow boundary beneath Campi Flegrei Caldera (Italy): Evidence for the magma chamber. *J. Geophys. Res.* **1992**, *97*, 15351–15359. [CrossRef]
61. Benoit, J.P.; McNutt, S.R. New constraints on source processing of volcanic tremor at Arenal Volcano, Costa Rica, using broadband seismic data. *Geophys. Res. Lett.* **1997**, *24*, 449–452. [CrossRef]
62. Peterson, J. *Observation and Modeling of Seismic Background Noise*; US Geological Survey Open File Report; US Geological Survey: Albuquerque, NM, USA, 1993; pp. 93–322.
63. Cosentino, M.; Lombardo, G.; Privitera, E. A Model for Internal Dynamic Processes on Mt. Etna. *Geophys. J.* **1989**, *97*, 367–379. [CrossRef]
64. Hirn, A.; Nicolich, R.; Gallart, J.; Laigle, M.; Cernobori, L.; ETNASEIS Scientific Group. Roots of Etna volcano in faults of great earthquakes. *Earth Planet. Sci. Lett.* **1997**, *148*, 171–191. [CrossRef]
65. Villaseñor, A.; Benz, H.M.; Filippi, L.; De Luca, G.; Scarpa, R.; Patanga, G.; Vinciguerra, S. Three-dimensional P-wave velocity structure of Mt. Etna, Italy. *Geophys. Res. Lett.* **1998**, *25*, 1975–1978. [CrossRef]
66. Bonforte, A.; Puglisi, G. Dynamics of the eastern flank of Mt. Etna volcano (Italy) investigated by a dense GPS network. *J. Volcanol. Geotherm. Res.* **2006**, *153*, 357–369. [CrossRef]
67. Bonaccorso, A. Dynamic inversion of ground deformation data for modelling volcanic sources (Etna 1991–1993). *Geophys. Res. Lett.* **1996**, *23*, 451–454. [CrossRef]
68. Murru, M.; Console, R.; Falcone, G.; Montuori, C.; Sgroi, T. Spatial mapping of the b value at Mount Etna, Italy, using earthquake data recorded from 1999 to 2005. *J. Geophys. Res.* **2007**, *112*, B12303. [CrossRef]